Intranuclear Photosensitizer Delivery and Photosensitization for Enhanced Photodynamic Therapy with Ultralow Irradiance

*Limin Pan, Jianan Liu, and Jianlin Shi**

Photodynamic therapy (PDT) is a well-established clinical treatment modality for various diseases. However, reactive oxygen species (ROS) generated by photosensitizers(PS) under proper irradiation exhibits the extremely short life span (<200 ns) and severely limited diffusion distance (20 nm), so the damage of ROS to biomolecules, especially DNA, is strongly confined to the immediate vicinity of ROS generation. In this report, an efficient nuclear-targeted delivery strategy is proposed by using TAT and RGD peptides co-conjugated mesoporous silica nanoparticles (MSNs) as PS carriers. The conjugation of TAT peptides enable the nuclear penetration of MSNs for efficient accumulation of PS inside nuclei. The intranuclear-accumulated PS can generate ROS upon irradiation right inside nuclei to destroy DNA instantaneously. For the purpose of in vivo applications, the co-conjugated RGD peptides endow the nuclear-targeted delivery system with specific binding and recognition to tumor vasculature and tumor cell membranes for significantly enhanced specificity and reduced side effects. Through intravenous injection of these nanosystems in tumor-bearing mice at a rather low PS dose of 2 mg/kg, tumor growth is efficiently inhibited by an extremely low irradiation dose of 6 J/cm^2. This work presents a new paradigm for specific PDT with high efficacy and low side effects in vivo.

1. Introduction

As an emerging treatment protocol in cancer therapy, photodynamic therapy (PDT) presents a highly promising noninvasive therapeutic strategy using photosensitizers (PS) and light irradiation to induce cell death and tissue destruction.[1] Upon exposure to light in appropriate wavelength band, the PS can transfer energy to surrounding oxygen molecules and generate cytotoxic reactive oxygen species (ROS), such as singlet oxygen ($^1O_2$), superoxide, hydrogen peroxide and hydroxyl radicals, which ultimately eliminate highly proliferating cells by crucial and irreversible damage to biomolecules including DNA, proteins and lipids.[2] Compared to traditional chemotherapy and radiotherapy, PDT is featured with remarkably reduced side effects to normal tissues since the PS are usually nontoxic to cells in the absence of light irradiation.[3] Moreover, PDT does not result in scarring and can be treated with repeated doses without initiating resistance.[4] For these reasons, PDT has become a hot topic of the intensive investigation as a promising strategy for various cancers and also non-cancer lesions in recent years.[5]

However, the clinical application of classic PS-based PDT in tumor therapy, especially those developed in deep tissues, still suffers from several serious technical difficulties which are mostly associated with poor solubility and short lifetimes of PS under physiological conditions, low specificity of PS to tumor tissues, and the limited penetration depth of a sufficient number of photons through tissue.[1b,2a,6] The most important factor determining the outcome of PDT is the pathway of the PS interacting with cells within the target tissue or tumor, which is largely determined by the subcellular localization of the PS, since PS can be up-taken by different subcellular organelles such as the mitochondria, lysosomes, endoplasmic reticulum, Golgi apparatus and plasma membranes.[7] The DNA damage by PDT refers to the strand breaks and alkali-labile lesions in the DNA molecules and the inactivation of enzymes involved in DNA repair by ROS.[8] As ROS has an instantaneous lifetime of less than 200 ns and can only act in the immediate vicinity of the ROS generation due to the short diffusion range (approximately 20 nm) during this period,[8,9] the ROS generation should be extremely restricted to the target molecules, that is, DNA helix. Therefore, instead of cell membranes and other cytoplasmic organelles, it is the cell nucleus that is known to be the much more sensitive and ideal sites for photodynamic damage.[10] Thus, an effective approach to enhance the photocytotoxicity of PS is the nuclear-targeted delivery of PS to the hypersensitive cell nucleus.[10b,c,11]

The direct intranuclear PS transport has been reported by the conjugation of PS to nuclear localization signals (NLS), which facilitated the nuclear penetration of PS, which maximally increased its photocytotoxicity over 2000-fold, highlighting the nuclear targeting approach for enhanced photodynamic efficiency.[12] Unfortunately, the in vivo use of these

Dr. L. Pan, Dr. J. Liu, Prof. J. Shi
State Key Laboratory of High Performance Ceramics and Superfine Microstructure
Shanghai Institute of Ceramics
Chinese Academy of Sciences
1295 Ding-Xi Road, Shanghai 200050, China
E-mail: jlshi@mail.sic.ac.cn

DOI: 10.1002/adfm.201402255

NLS-conjugated PS greatly suffers from a number of obstacles such as their nonspecific distributions in normal tissues, environmental degradation, hydrophobicity, and so on.[13]

Thanks to the development of nanotechnology, direct PS delivery by drug delivery systems has been established by incorporating PS into various biocompatible delivery platforms such as microcapsules,[14] liposomes,[15] micelles[16] and metal nanoparticles,[17] which allow significant accumulation in tumors through the enhanced permeability and retention (EPR) effects.[18] Conjugating antibodies[19] or specific tumor-targeting moieties, for example, folic acid,[20] to the surface of nanoparticles further enhanced the selective accumulation of PS in tumor cells, leading to exceptional PDT efficacy both in vitro and in vivo.[10a] Previous studies have shown that mesoporous silica nanoparticles (MSNs) are potential carriers of PS for enhanced PDT[21] owing to their unique advantages such as large surface area and pore volume, tunable size distribution, and more importantly, the easy surface modification.[22] However, despite the cell-specific uptake of these nanocarriers, the nuclear localization of these heterogeneous nanoparticles for intranuclear PS delivery has not been realized to date because the nucleus is strictly separated from the rest of cell cytoplasm by the double membrane structure of the nuclear envelop, which is embedded with plenty of nuclear pore complexes (NPCs).[23] All of the exchanges between cytoplasm and nucleoplasm occurs through NPCs which are 20–70 nm in diameter.[23a,24] Therefore, small molecules are able to pass through NPCs via passive diffusion, but molecules >45kDa and heterogeneous nanoparticles require specific targeting signals to gain either access to or egress from the nucleus.[24,25] Consequently, there is an urgent need for the development of novel PS-nanomaterials formulation which is capable of not only recognizing tumor cells for enhanced cellular uptake and preventing non-specific uptake by normal cells, but also efficiently targeting nucleus for intranuclear photosensitization by the substantially enhanced amount of nuclear accumulation of PS and in situ ROS generation for DNA damage and PDT enhancement.

In this study, we demonstrate a novel kind of sequential-targeted PS delivery strategy based on MSNs which is capable of specifically targeting tumor vasculature and cell membrane, and subsequently targeting nuclear membrane for direct intranuclear photosensitization and remarkably enhanced intranuclear PDT at substantially reduced PS and light dosages. MSNs hold several advantages over traditional organic polymeric particles for loading PS, such as relatively easy and accurate controls over the particle morphology, mesoporosity and sizes (e.g., up to smaller than 50 nm), and the high chemical and biological stability against to changes in pH and microbial attack. To apply the nanoformulation for intranuclear photosensitization and efficient PDT by in situ generated ROS right inside nuclei and instantaneous DNA damage, we propose a simple approach for constructing targeted PS delivery system using small sized MSNs functionalized with RGD peptides for vasculature and cell membrane targeting and TAT peptides for subsequent nuclear targeting (**Scheme 1**). This developed nuclear targeted PDT platform bestows several characteristics: i) significantly enhanced accumulation at tumor site and subsequent cellular uptake due to the specific binding

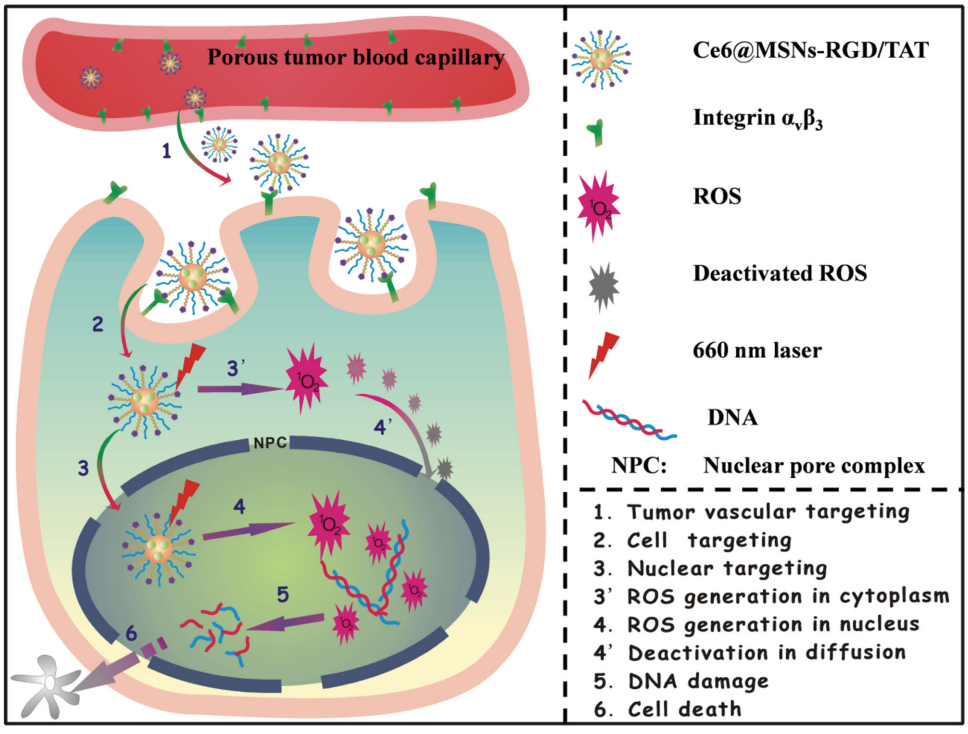

Scheme 1. Schematic illustration of sequential-targeted PDT based on Ce6@MSNs-RGD/TAT. Tumor vasculature targeting mediated by RGD peptides for enhanced intratumoral accumulation and retention of Ce6@MSNs-RGD/TAT during blood circulation. Cancer cell membrane targeting by the specific binding of RGD peptides to integrin $\alpha_v\beta_3$ over-expressed on the cell membrane. Nuclear targeting enabled by TAT peptides for intranuclear delivery of the photosensitizer Ce6 by Ce6@MSNs-RGD/TAT. The ROS directly generated inside nuclei could destroy DNA instantaneously for remarkably enhanced cell death without deactivation of cytoplasm-generated ROS on the way of diffusion towards nuclei.

between RGD peptides and integrin $\alpha_v\beta_3$ which is overexpressed on angiogenic endothelial cells as well as various malignant tumor cells, such as breast and prostate tumors, ovarian carcinoma, glioblastoma, and malignant melanoma; ii) dramatically increased intranuclear PS accumulation and in situ ROS generation to destroy DNA instantaneously and enhanced cell killing; iii) extraordinarily high inhibition rate of tumor growth at extremely low photo irradiation power density with negligible side effects. Therefore, the unique tumor targeting and intranuclear penetration make the synthesized MSNs-RGD/TAT a promising PDT platform of high efficacy and reduced adverse effects.

2. Results and Discussion

2.1. Synthesis and Characterization

Taking into consideration that chlorin e6 (Ce6) is a negatively charged PS with poor solubility, positively charged MSNs were synthesized by traditional Stöber protocol with surface modification as shown in **Figure 1**a. Ultrasmall MSNs with amine functionalized both on outer surface and pore walls were prepared by the co-condensation of silane coupling agent (APTES) and silica precursor (TEOS) under basic conditions. The amino

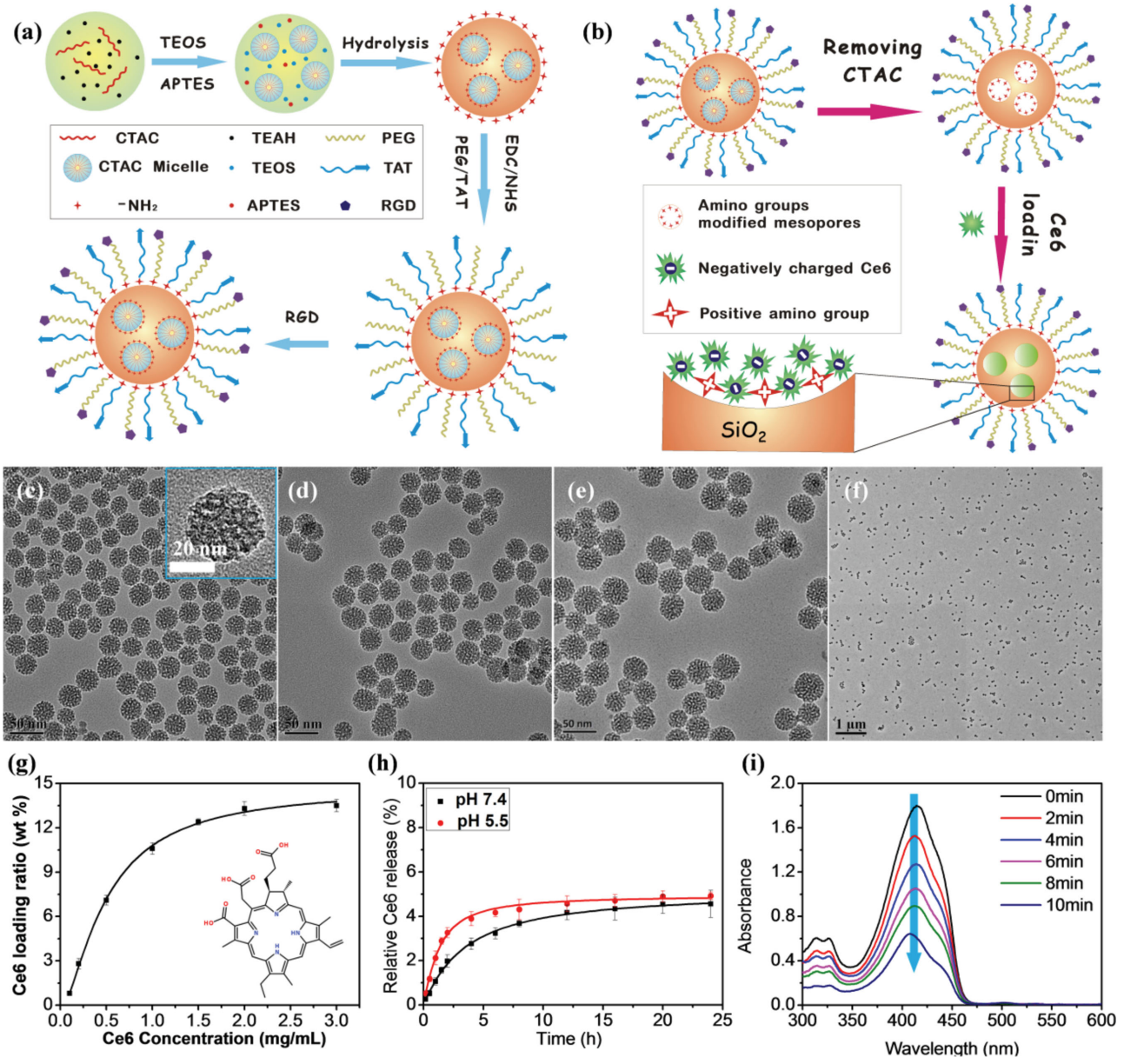

Figure 1. Characterization of the chemical and physical properties of MSNs-based nanomaterials. a) Schematic illustration of the synthesis of MSNs-RGD/TAT. b) Schematic illustration of Ce6 loading. Transmission electron microscopic (TEM) images of c) MSNs, d) MSNs-RGD, e) MSNs-RGD/TAT, and f) low magnification of MSNs-RGD/TAT. g) Ce6 loading capacity as a function of Ce6 feeding concentration. Insert: Chemical formula of Ce6. h) Release of Ce6 from MSNs-RGD/TAT in PBS at different pH values. i) UV–Vis spectra of DPBF as a sensor for detecting the ROS generation from Ce6@MSNs-RGD/TAT under 660 nm laser irradiation at 50 mW/cm^2.

groups are very beneficial to the co-conjugation of RGD and TAT peptides on the surface of MSNs before the removal of templates inside mesopores (Figure 1a). At the same time, after the extraction of surfactants, the high positive charge density of amine groups in the mesopores generated a strong electrostatic attraction between the silica walls and the negative (acidic) groups of Ce6 for efficient Ce6 loading (Figure 1b). Transmission electron microscopic (TEM) images show that the one-pot synthesized positive MSNs are in high uniformity with an average particle diameter about 30 nm (Figure 1c), which could also be found in scanning electron microscopic (SEM) images in different magnifications (Figure S1, Supporting Information). The textural properties of MSNs were analyzed by N_2 adsorption–desorption isotherms (Figure S2, Supporting Information), which gave a Brunauer-Emmett-Teller surface area of 674 m^2/g and a well-defined pore size of ≈3.1 nm. Before the removal of templates, RGD and TAT peptides were conjugated to the out surface of MSNs covalently (Figure S3, Supporting Information). Conjugation of RGD and TAT peptides were monitored by UV–Vis absorbance spectrometry (Figure S4, Supporting Information), which shows the peaks corresponding to RGD and TAT peptides at 275 nm and 490 nm, respectively. From TEM images (Figure 1d,e), the conjugation of peptides onto MSNs does not appear to affect the size of nanoparticles while the average hydrodynamic size of these nanoparticles measured by dynamic light scattering (DLS) technique does increase from 38.6 nm to 45.7 nm which is understandable due to the interaction between water molecules and peptides grafted on the outer surface of nanoparticles (Figure S5, Supporting Information). Furthermore, the zeta potential (Figure S6, Supporting Information) of all nanoparticles were measured, which indicate that the positive charging results directly from the functionalization of MSNs. This phenomenon provides additional evidence for the successful conjugations of RGD and TAT peptides. Then surfactants were then extracted by stirring in methanol with 1 wt% NaCl to expose amine groups on mesopore walls for Ce6 loading. Negatively charged Ce6 molecules were loaded into MSNs-RGD/TAT by mixing nanoparticles with different concentrations of Ce6 in dimethylsulfoxide (DMSO) under overnight stirring, free Ce6 were removed by centrifugation and successful Ce6 loading in nanoparticles was verified by the decrease in zeta potential after Ce6 loading (Figure S6, Supporting Information). The loading capacity was calculated by using the UV–Vis absorption peak intensity at 404 nm of Ce6 in supernatant compared with the standard curve of free Ce6 in DMSO, and thus the relationship between the feeding concentration of Ce6 and the amount finally loaded into MSNs-RGD/TAT was obtained (Figure 1g). It can be found that the loading capacity of Ce6 reaches a maximum of 13% at Ce6 concentrations above 3 mg/mL which was then used in the following experiments. The release profiles of Ce6 from MSNs-RGD/TAT indicate very limited Ce6 release from the nanoformulation in phosphate-buffered saline (PBS) even at acidic pH due to the poor hydrophilicity of Ce6 (Figure 1h). This is favorable to avoid premature release in the blood stream for reduced side effects. The generation of singlet oxygen ($^1O_2$) under light irradiation was detected using the chemical trapping reagent 1,3-diphenylisobenzofuran (DPBF) whose absorbance at 410 nm would irreversibly decrease in the presence of $^1O_2$.[26] Figure 1i shows the decrease in absorbance intensity at 410 nm in Ce6@MSNs-RGD/TAT under 660 nm laser irradiation for varied exposure time durations. In the meantime, the singlet oxygen generation from free Ce6 was also assessed (Figure S7, Supporting Information) and the intensity changes at 410 nm absorption as a function of irradiation time were given in Figure S8 (Supporting Information). It is clear that singlet oxygen production efficiency of Ce6 is not significantly lowered by its incorporation within MSNs-RGD/TAT. In the case of DMSO containing only DPBF and MSNs-RGD/TAT separately (Figure S9,S10, Supporting Information), there was no change in the absorbance value at 410 nm under the same irradiation conditions, indicating that the decrease in the absorbance in the presence of Ce6 was solely caused by the generated singlet oxygen rather than by the irradiation itself or the nanocarriers. The $^1O_2$ generation efficiency of Ce6 loaded in MSNs-RGD/TAT allows us to use the nanoformulation for PDT treatment of cancer cells.

2.2. Selectivity of Ce6@MSNs-RGD/TAT

To understand the cellular and nuclear uptake behaviors of MSNs-RGD/TAT, HeLa cells were incubated with MSNs, MSNs-RGD and MSNs-RGD/TAT (60 μg/mL) for 12 h, and then imaged under a confocal laser scanning microscope (CLSM) (**Figure 2**a). To visualize the location of MSNs in subcellular level, rhodamine isothiocyanate (RITC) was attached covalently onto the silica pore walls via our reported procedure.[27] In the absence of RGD peptides, a weak red fluorescent signal could be found in cytoplasm indicating that MSNs could hardly be uptaken into the cells (Figure 2a1). On the contrary, MSNs-RGD could enter the cells much more efficiently due to the specific targeting effect of RGD peptides to integrin $\alpha_v\beta_3$ overexpressed on HeLa cell membrane leading to a significant enhancement in the red fluorescent signal from MSNs-RGD in cytoplasm (Figure 2a2). This proves that the presence of RGD peptides has endowed the nanoformula with significant PDT selectivity to recognize cancer cells. Importantly, the red spots in the nuclear region indicate that MSNs-RGD/TAT have successfully penetrated into nuclei (Figure 2a3). The co-conjugation of TAT peptides plays a decisive role in nuclear targeting procedure, in accordance with our previous researches.[28] These results are also confirmed by Bio-TEM imaging which clearly shows the nuclear distribution of MSNs-RGD/TAT (Figure 2b3,b4) compared with the cytoplasm uptake of MSNs (Figure 2b1) and MSNs-RGD (Figure 2b2). These data demonstrate the effectiveness of MSNs-RGD/TAT as both cell-specific and nuclear targeting vehicles for the intranuclear delivery of locally acting PS. The quantifications of cellular and nuclear uptakes of nanoparticles (Figure S11, Supporting Information), determined by ICP-AES measurements of the silicon contents, further demonstrates that MSNs-RGD can specifically target HeLa cells under the mediation by the RGD receptor, resulting in remarkably enhanced cellular uptake (7 times of that of naked MSNs). Furthermore, MSNs-RGD/TAT demonstrates both enhanced cellular uptake and, especially, greatly promoted nuclear penetration (50 times of that of MSNs-RGD). In addition, in order to demonstrate the tumor specificity of MSNs-RGD/TAT, distributions of nanoparticles in normal

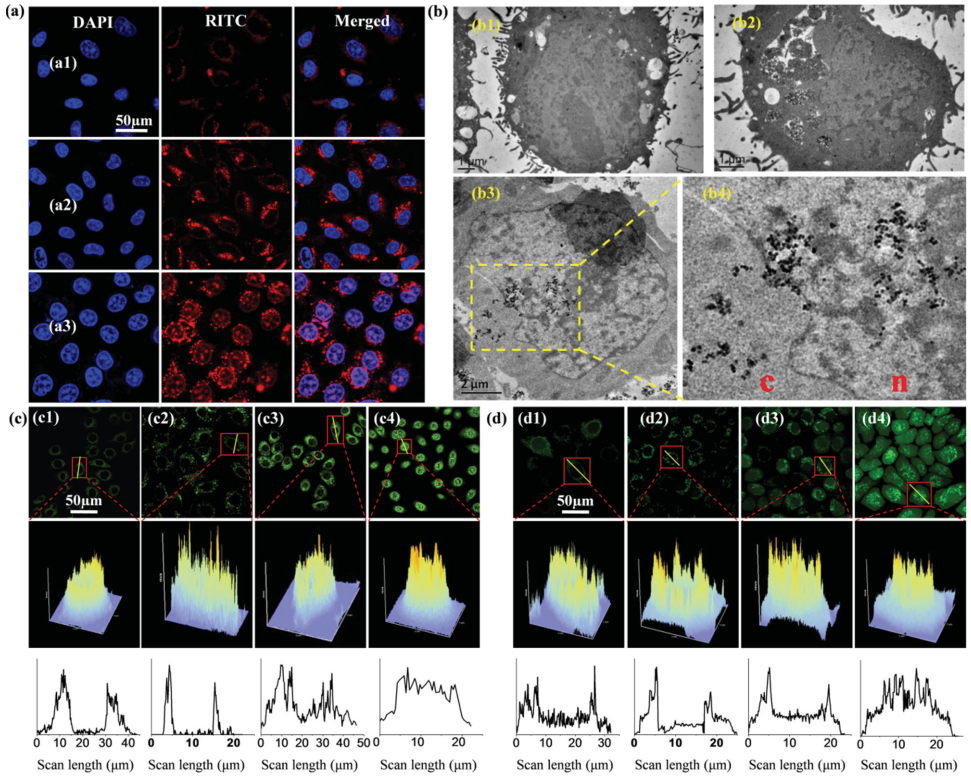

Figure 2. a) Confocal laser scanning microscopic (CLSM) images of HeLa cells incubated with a1) MSNs, a2) MSNs-RGD, a3) MSNs-RGD/TAT at the concentration of 60 μg/mL for 12 h. For each panel, the images from left to right show cell nuclei stained by DAPI (blue: DAPI = 4′,6-diamidino-2-phenylindole), RITC fluorescence from MSNs in cells (red), and overlays of the former two images. b) Bio-TEM images of HeLa cells incubated with b1) MSNs, b2) MSNs-RGD, b3) MSNs-RGD/TAT at the concentration of 60 μg/mL for 12 h. b4) Magnified area in (b3) for the visualization of nuclear penetration of MSNs-RGD/TAT. c = cytoplasm, n = nucleoplasm. c) Distribution of Ce6 in subcellular level observed by CLSM. HeLa cells incubated with c1) free Ce6, c2) Ce6@MSNs, c3) Ce6@MSNs-RGD, and(c4) Ce6@MSNs-RGD/TAT at the concentration of 1 μg/mL (with respect to Ce6) for 12 h. d) Subcellular location of ROS generated by Ce6 under irradiation of 660 nm at 6 J cm^{-2} using DCFH-DA staining. HeLa cells incubated with d1) free Ce6, d2) Ce6@MSNs, d3) Ce6@MSNs-RGD, and d4) Ce6@MSNs-RGD/TAT at the concentration of 1 μg/mL (with respect to Ce6) for 12 h. For (c,d): top panel: CLSM images of Ce6 or ROS; middle panel: 2D mappings of fluorescence of selected cells; bottom panel: line scanning profiles on selected cells. All CLSM images share the same scale bar (50 μm).

human embryonic kidney 293T cells with low $\alpha_v\beta_3$ integrin expression were observed (Figure S12, Supporting Information). It is clear that both the cellular and nuclear uptakes of MSNs-RGD/TAT are much lower in the normal cells due to the absence of cellular targeting effect of the nanoparticles to these cells, which indicates a substantially suppressed or even minimized interaction of the nanoparticles with the normal tissues in human physiological environment.

To demonstrate the cell-specific nuclear targeted delivery of Ce6, CLSM studies were performed on HeLa cells treated with free Ce6, Ce6@MSNs, Ce6@MSNs-RGD and Ce6@MSNs-RGD/TAT. As expected, owing to the nuclear penetration of MSNs-RGD/TAT, the fluorescence signal from Ce6 spread mainly in cell nuclei indicating the deep intranuclear location of Ce6@MSNs-RGD/TAT (Figure 2c4). The highly concentrated fluorescent signal inside the nuclei from the 2D mapping and line scanning profile of the selected cell further confirms the intranuclear delivery of Ce6. In contrast, free Ce6, Ce6@MSNs and Ce6@MSNs-RGD were found mainly in the cytoplasm (Figure 2c1–3), implying the indispensible role of TAT conjugation for intranuclear delivery. We further isolated cell nuclei to determine the amount of Ce6 accumulated in the nuclei (Figure S13, Supporting Information). It can be found that Ce6@MSNs-RGD/TAT transports greater than 45% of the total cellular uptaken Ce6 into the cell nuclei. In comparison, when the same amount of total Ce6 cells were treated with free Ce6, Ce6@MSNs and Ce6@MSNs-RGD under the same condition (with respect to Ce6), little Ce6 accumulation can be found in the cell nuclei. Taken together, we conclude that the nuclear uptake of Ce6@MSNs-RGD/TAT by HeLa cells is quite efficient even at low dosage.

To clarify the role of ROS in the nuclear targeted PDT, HeLa cells treated with Ce6@MSNs-RGD/TAT were stained with a ROS probe, DCFH-DA (2′,7′-dichlorodihydrofluorescein diacetate). This probe is nonfluorescent, but its oxidized product by ROS (DCF) could emit a green fluorescence.[29] The ROS level in cells was also observed after the cellular and nuclear uptakes of Ce6, Ce6@MSNs, Ce6@MSNs-RGD and Ce6@MSNs-RGD/TAT under irradiation. As shown in Figure 2d, much enhanced ROS signal intensity can be detected inside cell nuclei when cells were treated with Ce6@MSNs-RGD/TAT compared with free Ce6, Ce6@MSNs and Ce6@MSNs-RGD. These results clearly prove our expectation of the direct intranuclear ROS generation by nuclear-targeted delivery of Ce6.

2.3. In Vitro PDT on HeLa Cells

The in vitro phototoxicity study was carried out with a 660 nm laser operated at a power density of as low as 0.02 W/cm^2 for 5 min (light dose = 6 J/cm^2). Differently treated HeLa cells before and after the irradiation were characterized by fluorescent microscopic imaging for the observation of cell morphology change, calcein AM and propidium iodide co-stained cells for differing living cells from dead ones and DAPI stained cell nuclei for the assessment of nuclear damage. First, no changes can be observed to cells treated only with 660 nm laser or with MSNs-RGD/TAT at the concentration of 60 μg/mL (Figure S14, Supporting Information), which indicate that the irradiation itself without Ce6 is non-phototoxic to cells and the MSNs-based nanocarriers themselves are safe for cells. From the fluorescent microscopic images (**Figure 3**i), it can be seen clearly that after irradiation, morphology of cells treated with Ce6@MSNs-RGD/TAT changed dramatically (Figure 3d), while free Ce6 and Ce6@MSNs has neglectable effects on HeLa cells (Figure 3a,b), and Ce6@MSNs-RGD without nuclear-targeting effect only leads to slight shrinkage of HeLa cells (Figure 3c). The fluorescent live-dead cells staining (Figure 3ii) further confirms these results which shows almost no live cells after the irradiation of the cells treated by Ce6@MSNs-RGD/TAT. The apparent difference in shape and morphology of cells at the boundary of light spot (Figure S15, Supporting Information) further demonstrates the significant phototoxicity of Ce6@MSNs-RGD/TAT. Eventually, the nuclear damages directly caused by PDT were also investigated in the CLSM study as the produced fragments of DAPI-stained nuclei in the HeLa cells would be clearly visible if killed. It is clear from Figure 3iii that the nuclei are fragmented most significantly by PDT using Ce6@MSNs-RGD/TAT. These nuclear fragments are most likely from an alteration in nucleotide hydrogen bonding and coding specificity caused by oxygen-free radicals, which will induce the chemical changes in the nucleotide moieties of DNA, such as C-Tor G-T transitions.[30] In contrast, the HeLa cells treated with free Ce6 and other non-nuclear-targeting groups keep their nuclei intact in their shapes after PDT (Figure 3iii). These results further confirm that the enhanced photocytotoxicity of Ce6@MSNs-RGD/TAT is due to the intranuclear localization of Ce6 via DNA damage by singlet oxygen generated on site.

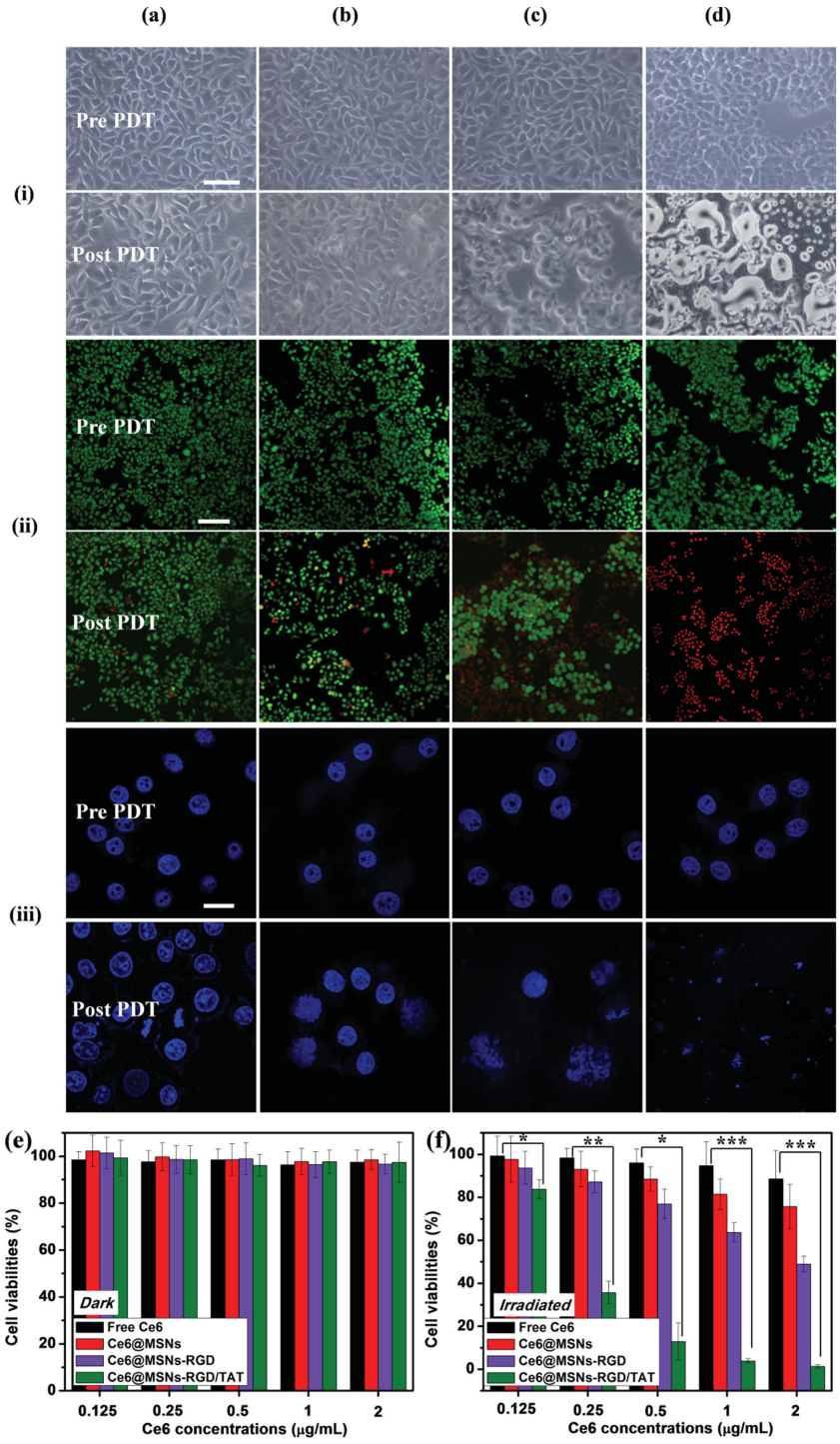

Figure 3. In vitro PDT effects on HeLa cells incubated with a) free Ce6, b) Ce6@MSNs, c) Ce6@MSNs-RGD, and d) Ce6@MSNs-RGD/TAT at the concentration of 1 μg/mL (with respect to Ce6) for 12 h. i) Fluorescence microscopic images of the cells before and after light irradiation. Scale bar: 50 μm. ii) CLSM images of calcein AM and propidium iodide co-stained cells before and after light irradiation. Live cells: green fluorescence of calcein AM; dead cells: red fluorescence of propidium iodide. Scale bar: 200 μm. iii) CLSM images of cell nuclei stained by DAPI for the assessment of nuclear damage before and after light irradiation. Scale bar: 20 μm. Cell viabilities of HeLa cells incubated with free Ce6, Ce6@MSNs, Ce6@MSNs-RGD, and Ce6@MSNs-RGD/TAT e) without and f) with light irradiation at varied Ce6 concentrations. (*p < 0.05, **p < 0.001, ***p < 0.0001) All of the PDT treatments were carried out using a 660 nm laser at light dose of 6 J/cm^2.

The standard methyl thiazolyl tetrazolium (MTT) assay was carried out to determine the relative viabilities of cells at 12 h post various treatments. Without light exposure, free Ce6, Ce6@MSNs, Ce6@MSNs-RGD and Ce6@MSNs-RGD/TAT exhibit negligible dark toxicity to HeLa cells (Figure 3g). As expected, when irradiated with 660 nm laser, the cancer killing effect by Ce6@MSNs-RGD/TAT is remarkably higher than those by either free Ce6, Ce6@MSNs or Ce6@MSNs-RGD at the identical Ce6 concentration of as low as 0.25 μg/mL (Figure 3h). In order to clarify the feasibility of intranuclear photosensitizer delivery and photosensitization upon different tumor models, PDT effects on human glioblastoma U87MG cells with high $\alpha_v\beta_3$ integrin expression have also been evaluated using the MTT assay (Figure S16,Supporting Information). The phototoxicity of Ce6@MSNs-RGD/TAT toward U87MG cells can be found significantly enhanced relative to free Ce6.

2.4. Cytotoxicity Evaluation of Ce6@MSNs-RGD/TAT Under PDT

Given that Ce6@MSNs-RGD/TAT was severely phototoxic to HeLa cells under PDT, we further investigated its performance at varied power densities and irradiation time durations. For each panel at a fixed power density, the fluorescent microscopic images of the same cells took along with the extension of irradiation time clearly show the morphology changes of the cells in the process of light exposure (**Figure 4**a). Obviously, the increase of power density will lead to enhanced phototoxicity because higher light energy input will generate more ROS at the same concentration of Ce6. Moreover, cell viability data confirm that Ce6@MSNs-RGD/TAT could induce cell death under extremely low light doses. More than half of cells are destroyed when exposed to 0.02 W/cm^2 for only 1 min. Even when the power density was

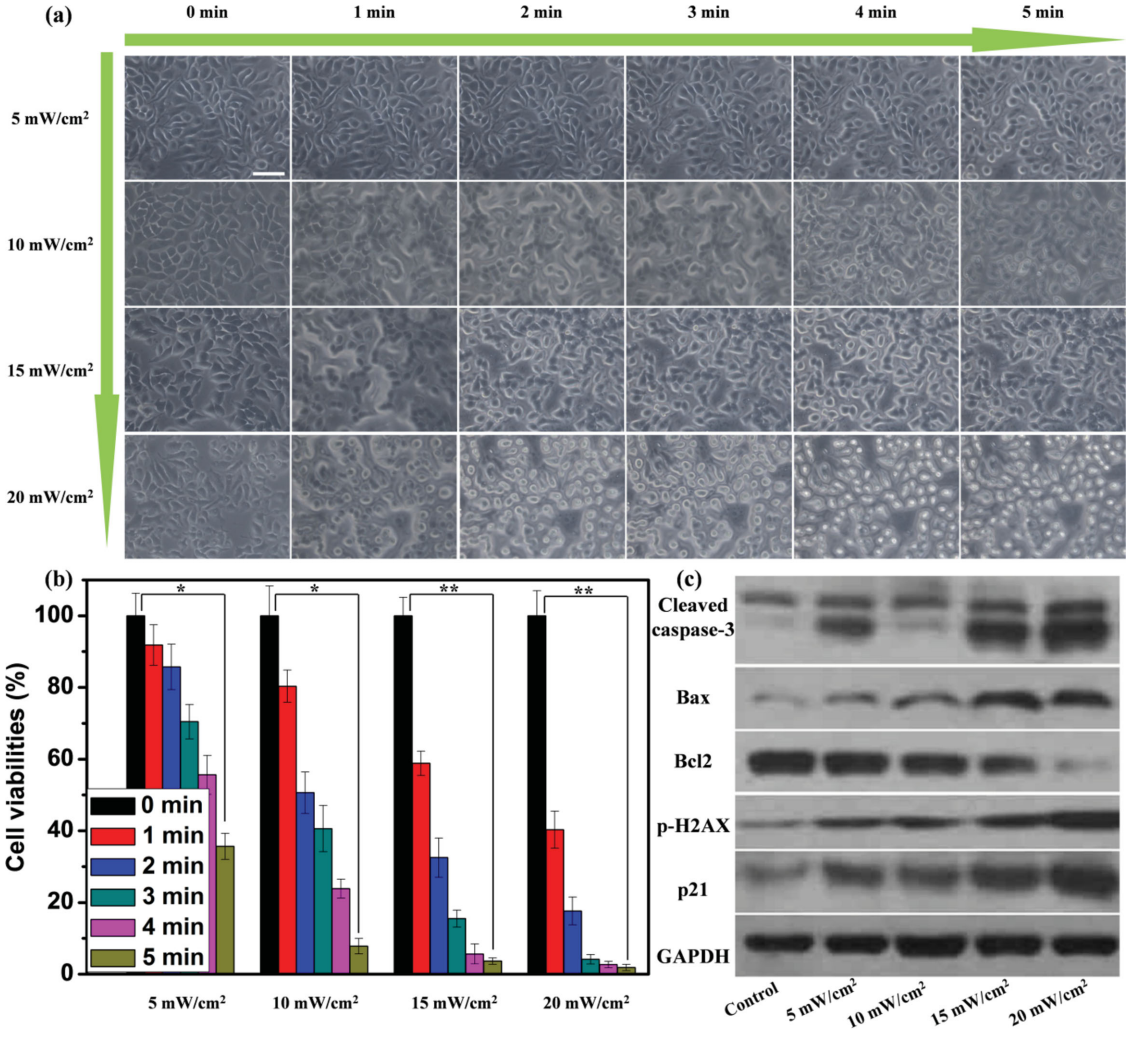

Figure 4. a) Fluorescence microscopic images of HeLa cells incubated with Ce6@MSNs-RGD/TAT at the concentration of 1 μg/mL for 12 h under irradiation at varied light intensities: 5 mW/cm^2, 10 mW/cm^2, 15 mW/cm^2, and 20 mW/cm^2 measured at 1 min, 2 min, 3 min, 4 min, and 5 min upon irradiation. (*$p < 0.05$, **$p < 0.001$) Scale bar: 50 μm. b) Viabilities of HeLa cells incubated with Ce6@MSNs-RGD/TAT for 12 h and under irradiation with 660 nm laser at different light dosages. c) Effects of nuclear targeted PDT on the expression of cleaved caspase-3, Bax/Bcl2, p-H2AX, and p21 after irradiation by 660 nm laser at 5 mW/cm^2, 10 mW/cm^2, 15 mW/cm^2, and 20 mW/cm^2 for 1 min.

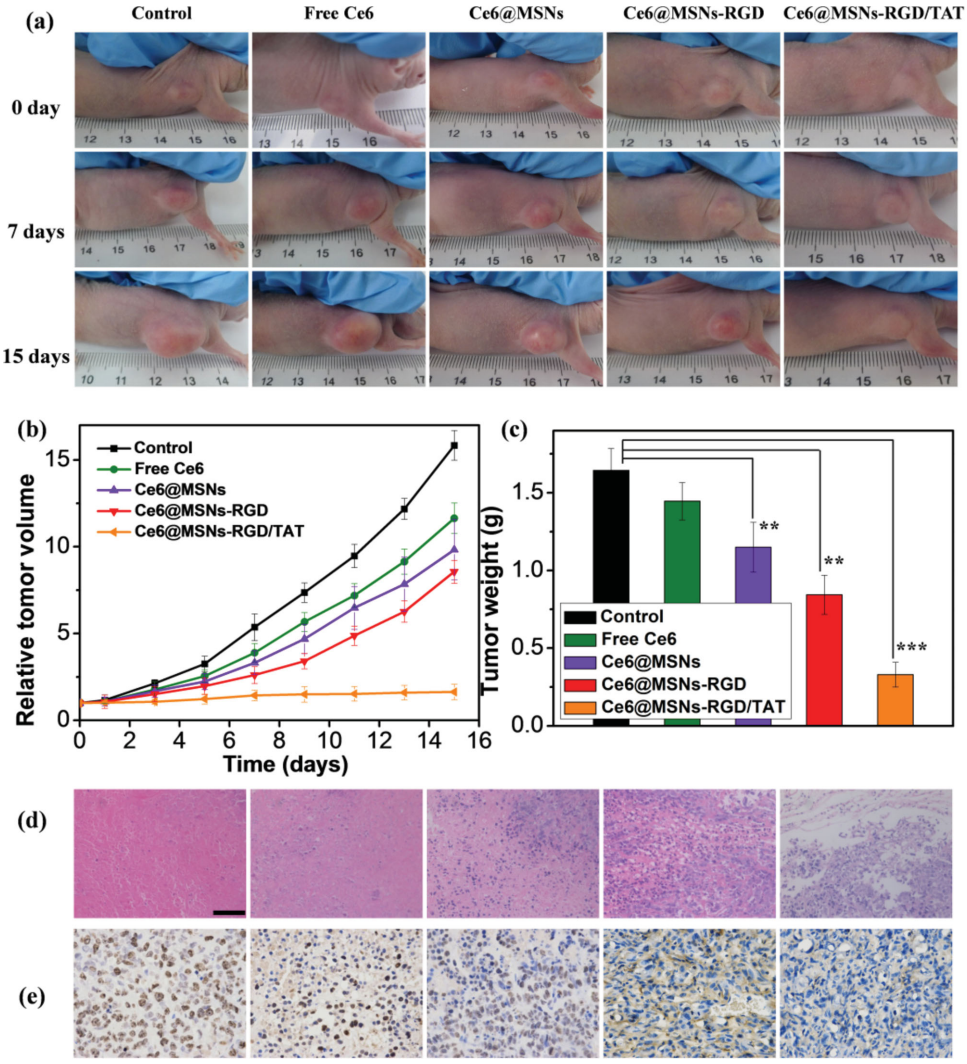

Figure 5. In vivo applications of Ce6@MSNs-RGD/TAT. a) Photographs of the mice taken before (0 day), in 7 and 15 days of PDT. Effects of PBS (control, 150 μL), free Ce6, Ce6@MSNs, Ce6@MSNs-RGD, and Ce6@MSNs-RGD/TAT on the growth of HeLa cancer xenografts upon treatment of 660 nm laser at 20 mW/cm^2 for 5 min. A dosage of 2 mg/kg (with respect to Ce6) was administrated intravenously for all mice (n = 6–8). b) Tumor growth curves of different groups of tumor-bearing mice after PDT. The tumor sizes were measured at the indicated time points. c) Tumor weight of mice in different groups after 15 days of PDT. Data are means ± s.d. (5 mice per group), $^{**}p < 0.001$, $^{***}p < 0.0001$ compared to other group using the Student's t test. d) H&E staining and e) immunohistochemical staining analysis for Ki67 of tumor sections collected from different groups of mice 7 days post PDT treatment. From left to right: tumor from mice treated with PBS, free Ce6, Ce6@MSNs, Ce6@MSNs-RGD and Ce6@MSNs-RGD/TAT. Scale bare: 100 μm.

further lowered to 0.005 W/cm^2, the survival ratio of HeLa cells is lower than 40% in 5 min irradiation (corresponding light dosage: 1.5 J/cm^2).

To better understand the apoptotic signaling pathway, we examined the expressions of apoptotic regulators in Ce6@MSNs-RGD/TAT-treated HeLa cells by western blot analysis. As shown in Figure 4c, pro-apoptotic protein cleaved caspase-3[31] and Bax expressions intensify in a dose-responsive manner in HeLa cells exposed to the laser of varied power densities, whereas that of anti-apoptotic protein Bcl2 decrease significantly. The expression of phosphorylated H2AX,[32] a marker of double-strand breaks, become dramatically stronger along with the increase of power density, and the cyclin-dependent kinase inhibitor p21,[33] an important regulator of cell cycle progression, senescence and differentiation, also largely levels up. These results should be the consequence of oxidative damage to the DNA helix caused by the intranuclear accumulation of Ce6 mediated by MSNs-RGD/TAT and the subsequent in situ ROS generation.

2.5. In Vivo PDT on Subcutaneous HeLa Tumor Bearing Mice

The in vivo antitumor activities were compared using a HeLa tumor xenograft model. Mice bearing the tumors were intravenously injected with PBS, free Ce6, Ce6@MSNs, Ce6@MSNs-RGD and Ce6@MSNs-RGD/TAT at a Ce6-equivalent dose of 2 mg/kg. From the digital photos of tumors (**Figure 5**a), it is apparent that the treatment with free Ce6 leads to slight

inhibition of tumor growth compared to the control group (PBS). The inhibition of tumor growth was slightly enhanced by treating with Ce6@MSNs compared to free Ce6. The relatively stronger antitumor effect of Ce6@MSNs-RGD suggests the importance of cell targeting of the nanoformula. Remarkably, Ce6@MSNs-RGD/TAT induces substantially stronger tumor growth inhibition effect than Ce6@MSNs-RGD, Ce6@MSNs and free Ce6. The relative tumor volume curves prove much more efficient in vivo PDT effects of Ce6@MSNs-RGD/TAT (Figure 5b) than the others. According to the weight changes of tumors, the inhibition rates of free Ce6, Ce6@MSNs, Ce6@MSNs-RGD and Ce6@MSNs-RGD/TAT are 16.5%, 30%, 46.9% and 80.5%, respectively (Figure 5c). Furthermore, the treatment efficacy in terms of tumor cell death was also evaluated by histological analysis of tumor tissue from different treatment groups in 7 days after the treatments (Figure 5d). In the control group, the tumor tissue sections are composed of tightly packed tumor cells while apoptotic tumor cells can be hardly observed. After the treatment with Ce6@MSNs-RGD/TAT, prominent necrosis can be found, indicating the successful destruction of tumor cells. The tumors treated with Ce6@MSNs-RGD/TAT show significantly lower tumor cellularity and more vacuolization than those treated with free Ce6, Ce6@MSNs and Ce6@MSNs-RGD, which is consistent with the higher inhibition rate on tumor growth induced by Ce6@MSNs-RGD/TAT than those by free Ce6, Ce6@MSNs and Ce6@MSNs-RGD. Meanwhile, the immunohistochemical staining of tumor section for antigen Ki67 was used for the evaluation of cell proliferation (Figure 5e). The expression of antigen Ki67 was positive as brown granules in the cell nucleus. As it is expected, the tumor cells after treatment of Ce6@MSNs-RGD/TAT is much less than other groups. These results clearly suggest that the direct intranuclear delivery of Ce6 by MSNs-RGD/TAT results in much higher anticancer efficiency than other delivery system, which holds great potential in future cancer treatment.

The potential in vivo toxicity or side effects is always a great concern for PDT agents used in clinical application.[34] To verify the applicability of Ce6@MSNs-RGD/TAT in vivo, the mice treated with PDT by Ce6@MSNs-RGD/TAT and irradiation were examined. The mice show slight and steady body weight gain during 15 days after the treatment (Figure S17, Supporting Information). From H&E staining of organ slices (Figure S18, Supporting Information), neither noticeable sign of organ damage nor inflammation can be observed at elevated Ce6 dose of 2 mg/kg in comparison with the control group, suggesting the negligible side effects of Ce6@MSNs-RGD/TAT in in vivo PDT. Moreover, the blood analysis (Figure S19, Supporting Information) in different intervals after the intravenous injection of MSNs-RGD/TAT indicates no visible hepatic and kidney disorder of mice by MSNs-RGD/TAT. In addition, compared with the control group, all parameters of a complete blood panel are in normal states. Therefore, the nuclear-targeting MSNs-based nanocarriers are favorable for in vivo photodynamic treatment of cancer with much enhanced PDT efficacy on tumors but no significant side effects to normal organs of the treated mice. These observations have significant implications for efficient and safe PDT in future clinical applications.

3. Conclusion

We have designed and demonstrated a MSNs-based intranuclear photosensitization nanosystem by sequential vascular-cellular-nuclear-targeted photosensitizer delivery, which exhibits intranuclear ROS generation and in situ DNA damage property leading to greatly enhanced photodynamic therapeutic effect at an extremely low light doses of <6 J/cm^2 (0.02 W/cm^2 for 5 min). By the tumor vasculature targeting, the accumulation and retention of the nanoformulation are effectively enhanced during blood circulation, and the subsequent cancer membrane targeting property contributes considerably to the increased cellular uptake of these agents which ensure the high level of photosensitizer inside cells. Finally, the nuclear targeting peculiarity enables the efficient nuclear accumulation of photosensitizer and then ROS generation around DNA helix under irradiation which plays a key role in maximizing the utilization of ROS for DNA oxidation in their extremely limited life span and diffusion distance. We anticipate a promising future of this nanosystem featured with direct intranuclear photosensitizer delivery, with its excellent photocytotoxicity under faint light irradiation for fighting deep-seated tumors.

Supporting Information

Supporting Information is available from the Wiley Online Library or from the author.

Acknowledgements

This work was financially supported by National Natural Science Foundation of China (Grant No. 51132009, 51102259).

Received: July 8, 2014
Revised: August 11, 2014
Published online: September 30, 2014

[1] a) D. K. Chatterjee, L. S. Fong, Y. Zhang, *Adv. Drug Delivery Rev.* **2008**, *60*, 1627–1637; b) J. F. Lovell, T. W. B. Liu, J. Chen, G. Zheng, *Chem. Rev.* **2010**, *110*, 2839–2857.
[2] a) J. P. Celli, B. Q. Spring, I. Rizvi, C. L. Evans, K. S. Samkoe, S. Verma, B. W. Pogue, T. Hasan, *Chem. Rev.* **2010**, *110*, 2795–2838; b) C. M. Moore, D. Pendse, M. Emberton, *Nat. Clin. Pract. Urol.* **2009**, *6*, 18–30.
[3] P. Agostinis, K. Berg, K. A. Cengel, T. H. Foster, A. W. Girotti, S. O. Gollnick, S. M. Hahn, M. R. Hamblin, A. Juzeniene, D. Kessel, M. Korbelik, J. Moan, P. Mroz, D. Nowis, J. Piette, B. C. Wilson, J. Golab, *CA: Cancer J. Clin.* **2011**, *61*, 250–281.
[4] D. E. J. G. J. Dolmans, D. Fukumura, R. K. Jain, *Nat. Rev. Cancer* **2003**, *3*, 380–387.
[5] Á. Juarranz, P. Jaén, F. Sanz-Rodríguez, J. Cuevas, S. González, *Clin. Transl. Oncol.* **2008**, *10*, 148–154.
[6] a) C. Wang, L. Cheng, Z. Liu, *Theranostics* **2013**, *3*, 317–330; b) R. Bonnett, *Chem. Soc. Rev.* **1995**, *24*, 19–33.
[7] S. Goel, F. Chen, W. Cai, *Small* **2014**, *10*, 631–645.
[8] S. H. Lim, C. Thivierge, P. Nowak-Sliwinska, J. Han, H. van den Bergh, G. Wagnières, K. Burgess, H. B. Lee, *J. Med. Chem.* **2010**, *53*, 2865–2874.
[9] S. Hatz, J. D. Lambert, P. R. Ogilby, *Photochem. Photobiol. Sci.* **2007**, *6*, 1106–1116.

[10] a) W. M. Sharman, J. E. van Lier, C. M. Allen, *Adv. Drug Delivery Rev.* **2004**, *56*, 53–76; b) A. A. Rosenkranz, D. A. Jans, A. S. Sobolev, *Immunol. Cell Biol.* **2000**, *78*, 452–464; c) Y. Takeuchi, K. Ichikawa, S. Yonezawa, K. Kurohane, T. Koishi, M. Nango, Y. Namba, N. Oku, *J. Controlled Release* **2004**, *97*, 231–240.

[11] R. Zhao, R. Hammitt, R. P. Thummel, Y. Liu, C. Turro, R. M. Snapka, *Dalton T.* **2009**, 10926–10931.

[12] a) T. V. Akhlynina, D. A. Jans, A. A. Rosenkranz, N. V. Statsyuk, I. Y. Balashova, G. Toth, I. Pavo, A. B. Rubin, A. S. Sobolev, *J. Biol. Chem.* **1997**, *272*, 20328–20331; b) S. K. Bisland, D. Singh, J. Gariépy, *Bioconjugate Chem.* **1999**, *10*, 982–992; c) T. V. Akhlynina, A. A. Rosenkranz, D. A. Jans, A. S. Sobolev, *Cancer Res.* **1995**, *55*, 1014–1019; d) T. V. Akhlynina, D. A. Jans, N. V. Statsyuk, I. Y. Balashova, G. Toth, I. Pavo, A. A. Rosenkranz, B. S. Naroditsky, A. S. Sobolev, *Int. J. Cancer* **1999**, *81*, 734–740; e) N. El-Akra, A. Noirot, J.-C. Faye, J.-P. Souchard, *Photochem. Photobiol. Sci.* **2006**, *5*, 996–999.

[13] Y. N. Konan, R. Gurny, E. Allémann, *J. Photochem. Photobiol. B* **2002**, *66*, 89–106.

[14] K. Wang, Q. He, X. Yan, Y. Cui, W. Qi, L. Duan, J. Li, *J. Mater. Chem.* **2007**, *17*, 4018–4021.

[15] A. S. Derycke, P. A. de Witte, *Adv. Drug Delivery Rev.* **2004**, *56*, 17–30.

[16] C. F. van Nostrum, *Adv. Drug Delivery Rev.* **2004**, *56*, 9–16.

[17] a) B. Tian, C. Wang, S. Zhang, L. Feng, Z. Liu, *ACS Nano* **2011**, *5*, 7000–7009; b) Y. Cheng, A. C. Samia, J. D. Meyers, I. Panagopoulos, B. Fei, C. Burda, *J. Am. Chem. Soc.* **2008**, *130*, 10643–10647; c) D. Bechet, P. Couleaud, C. Frochot, M.-L. Viriot, F. Guillemin, M. Barberi-Heyob, *Trends Biotechnol.* **2008**, *26*, 612–621.

[18] V. Torchilin, *Adv. Drug Deliver. Rev.* **2011**, *63*, 131–135.

[19] Y.-A. Shieh, S.-J. Yang, M.-F. Wei, M.-J. Shieh, *ACS Nano* **2010**, *4*, 1433–1442.

[20] S.-J. Yang, F.-H. Lin, H.-M. Tsai, C.-F. Lin, H.-C. Chin, J.-M. Wong, M.-J. Shieh, *Biomaterials* **2011**, *32*, 2174–2182.

[21] a) H. L. Tu, Y. S. Lin, H. Y. Lin, Y. Hung, L. W. Lo, Y. F. Chen, C. Y. Mou, *Adv. Mater.* **2009**, *21*, 172–177; b) C. Chen, L. Zhou, J. Geng, J. Ren, X. Qu, *Small* **2013**, *9*, 2793–2800; c) I. Roy, T. Y. Ohulchanskyy, H. E. Pudavar, E. J. Bergey, A. R. Oseroff, J. Morgan, T. J. Dougherty, P. N. Prasad, *J. Am. Chem. Soc.* **2003**, *125*, 7860–7865; d) J. Tu, T. Wang, W. Shi, G. Wu, X. Tian, Y. Wang, D. Ge, L. Ren, *Biomaterials* **2012**, *33*, 7903–7914; e) M. Gary-Bobo, Y. Mir, C. Rouxel, D. Brevet, I. Basile, M. Maynadier, O. Vaillant, O. Mongin, M. Blanchard-Desce, A. Morère, M. Garcia, J.-O. Durand, L. Raehm, *Angew. Chem. Int. Ed.* **2011**, *123*, 11627–11631.

[22] a) Slowing II, J. L. Vivero-Escoto, C. W. Wu, V. S. Y. Lin, *Adv. Drug Delivery Rev.* **2008**, *60*, 1278–1288; b) F. Tang, L. Li, D. Chen, *Adv. Mater.* **2012**, *24*, 1504–1534; c) Z. Li, J. C. Barnes, A. Bosoy, J. F. Stoddart, J. I. Zink, *Chem. Soc. Rev.* **2012**, *41*, 2590–2605; d) P. Yang, S. Gai, J. Lin, *Chem. Soc. Rev.* **2012**, *41*, 3679–3698; e) Q. Zhang, F. Liu, K. T. Nguyen, X. Ma, X. Wang, B. Xing, Y. Zhao, *Adv. Funct. Mater.* **2012**, *22*, 5144–5156; f) Y. Chen, H. Chen, J. Shi, *Adv. Mater.* **2013**, *25*, 3144–3176; g) Q. He, J. Shi, *J. Mater. Chem.* **2011**, *21*, 5845–5855.

[23] a) S. R. Wente, *Science* **2000**, *288*, 1374–1377; b) K.-H. Chow, R. E. Factor, K. S. Ullman, *Nat. Rev. Cancer* **2012**, *12*, 196–209.

[24] M. Belting, S. Sandgren, A. Wittrup, *Adv. Drug Delivery Rev.* **2005**, *57*, 505–527.

[25] a) K. M. Wagstaff, D. A. Jans, *Eur. J. Pharmacol.* **2009**, *625*, 174–180; b) T. M. Wheeler, A. J. Leger, S. K. Pandey, A. R. MacLeod, M. Nakamori, S. H. Cheng, B. M. Wentworth, C. F. Bennett, C. A. Thornton, *Nature* **2012**, *488*, 111–115; c) C. W. Pouton, K. M. Wagstaff, D. M. Roth, G. W. Moseley, D. A. Jans, *Adv. Drug Delivery Rev.* **2007**, *59*, 698–717.

[26] K. Hayashi, M. Nakamura, H. Miki, S. Ozaki, M. Abe, T. Matsumoto, T. Kori, K. Ishimura, *Adv. Funct. Mater.* **2013**, *24*, 503–513.

[27] Q. He, J. Shi, X. Cui, J. Zhao, Y. Chen, J. Zhou, *J. Mater. Chem.* **2009**, *19*, 3395–3403.

[28] a) L. Pan, Q. He, J. Liu, Y. Chen, M. Ma, L. Zhang, J. Shi, *J. Am. Chem. Soc.* **2012**, *134*, 5722–5725; b) L. Pan, J. Liu, Q. He, L. Wang, J. Shi, *Biomaterials* **2013**, *34*, 2719–2730.

[29] Q. He, J. Zhang, F. Chen, L. Guo, Z. Zhu, J. Shi, *Biomaterials* **2010**, *31*, 7785–7796.

[30] a) D. T. Ribeiro, R. C. De Oliveira, P. D. Mascio, C. F. Menck, *Free Radical Res.* **1994**, *21*, 75–83; b) D. I. Feig, T. M. Reid, L. A. Loeb, *Cancer Res.* **1994**, *54*, 1890s–1894s.

[31] G. M. Cohen, *Biochem. J.* **1997**, *326*, 1–16.

[32] E. P. Rogakou, D. R. Pilch, A. H. Orr, V. S. Ivanova, W. M. Bonner, *J. Biol. Chem.* **1998**, *273*, 5858–5868.

[33] Y. Xiong, G. J. Hannon, H. Zhang, D. Casso, R. Kobayashi, D. Beach, *Nature* **1993**, *366*, 701–704.

[34] a) J. Tian, L. Ding, H.-J. Xu, Z. Shen, H. Ju, L. Jia, L. Bao, J.-S. Yu, *J. Am. Chem. Soc.* **2013**, *135*, 18850–18858; b) K. Yang, H. Xu, L. Cheng, C. Sun, J. Wang, Z. Liu, *Adv. Mater.* **2012**, *25*, 5586–5592.